PAPER • OPEN ACCESS

The impact of $E \times B$ shear on microtearing based transport in spherical tokamaks

To cite this article: B.S. Patel *et al* 2025 *Nucl. Fusion* **65** 026063

OPEN ACCESS
IOP Publishing | International Atomic Energy Agency
Nuclear Fusion
Nucl. Fusion **65** (2025) 026063 (17pp)
https://doi.org/10.1088/1741-4326/ada627

The impact of $E \times B$ shear on microtearing based transport in spherical tokamaks

B.S. Patel[1,*], M.R. Hardman[1,2], D. Kennedy[1], M. Giacomin[3,4], D. Dickinson[4] and C.M. Roach[1]

[1] UKAEA (United Kingdom Atomic Energy Authority), Culham Campus, Abingdon, Oxfordshire OX14 3DB, United Kingdom of Great Britain and Northern Ireland
[2] Rudolf Peierls Centre for Theoretical Physics, University of Oxford, Oxford OX1 3PU, United Kingdom of Great Britain and Northern Ireland
[3] Dipartimento di Fisica 'G. Galilei', Università degli Studi di Padova, Padova, Italy
[4] University of York, Heslington, York YO10 5DD, United Kingdom of Great Britain and Northern Ireland

E-mail: bhavin.s.patel@ukaea.uk

Received 12 September 2024, revised 16 December 2024
Accepted for publication 6 January 2025
Published 31 January 2025

Abstract

Electromagnetic microtearing modes (MTMs) have been observed in many different spherical tokamak (ST) regimes. Understanding how these and other electromagnetic modes nonlinearly saturate is likely critical in understanding the confinement of a high β ST. Equilibrium $E \times B$ sheared flows have sometimes been found to significantly suppress low β ion scale transport in both gyrokinetic simulations and in experiment. This work aims to understand the conditions under which $E \times B$ sheared flow impacts on the saturation of MTM simulations, as there have been examples where it does (Guttenfelder *et al* 2012 *Phys. Plasmas* **19** 056119) and does not (Doerk et al 2012 *Phys. Plasmas* **19** 055907) have a considerable effect. Two experimental regimes are examined from MAST and NSTX, on surfaces that have unstable MTMs. The MTM driven transport on a local flux surface in MAST is shown to be more resilient to suppression via $E \times B$ shear, compared to the case from NSTX where the MTM transport is found to be significantly suppressed. This difference in the response to flow shear is explained through the impact of magnetic shear, $\hat{s}$, on the MTM linear growth rate dependence on ballooning angle, θ_0. At low $\hat{s}$, the growth rate depends weakly on θ_0, but at higher $\hat{s}$, the MTM growth rate peaks at $\theta_0 = 0$, with regions of stability at higher θ_0. Equilibrium $E \times B$ sheared flows act to advect the θ_0 of a mode in time, providing a mechanism to reduce the linear drive and suppress the transport from modes where the growth rate is strongly peaked in θ_0 (Roach *et al* 2009 *Plasma Phys. Control. Fusion* **51** 124020). Bicoherence analysis demonstrates that with the inclusion of $E \times B$ shear there is a more effective coupling between the linearly driven drift-waves responsible for transport and zonal modes, which enhances damping. The dependence of γ^{MTM} on θ_0 is in qualitative agreement with a recent theory (Hardman *et al* *Plasma Phys. Control. Fusion* **65** 045011) at low β when $q \sim 1$, but the agreement worsens at higher q where the theory breaks down. At higher $\hat{s}$, MTMs drive more

* Author to whom any correspondence should be addressed.

stochastic transport due a stronger overlap of magnetic islands centred on neighbouring rational surfaces, but equilibrium $E \times B$ shear acts to mitigate this. This is especially critical towards the plasma edge where $\hat{s}$ can be larger and where the total stored energy in the plasma is more sensitive to the local gradients. This work highlights the important role of the safety factor profile in determining the impact of equilibrium $E \times B$ shear on the saturation level of MTM turbulence.

Keywords: gyrokinetics, spherical tokamak, microtearing modes, turbulence

(Some figures may appear in colour only in the online journal)

1. Introduction

Microtearing modes (MTMs) have been observed in gyrokinetic simulations of various conceptual spherical tokamak (ST) designs [1–4] and in existing experiments in both the core [5–8] and the pedestal [9, 10]. These electromagnetic modes predominantly drive electron heat transport and can be destabilised by electron collisions [11], which has been proposed as a candidate explanation for the $B\tau_E \propto \nu_{ee}^{-0.82}$ scaling seen in STs [7, 12], with support from nonlinear gyrokinetic simulations of MTM turbulence [13]. It is computationally challenging to achieve well converged saturated nonlinear simulations of MTM turbulence, but several such simulations suggest MTMs may play a significant transport role in STs [14, 15], and close to the edge in conventional aspect ratio devices when in H-mode [10, 16]. To develop much needed reduced transport models for MTM turbulence with predictive power, it is important to understand the saturation mechanisms. There have been limited studies using simulations, and here we seek to explain the impact of flow shear on MTM turbulence.

For instabilities such as the ion temperature gradient (ITG) mode and kinetic ballooning mode (KBM), $E \times B$ shear can reduce the turbulent transport [17, 18]. This work aims to understand when $E \times B$ shear is relevant in suppressing MTM transport. $E \times B$ shear decorrelates turbulent eddies by tilting and shearing them radially, effectively adding a time dependence to their radial wavenumber k_x. One method to estimate the impact of flow shear on a mode is based on the dependence of its linear growth rate on the mode's radial wavenumber at the outboard mid-plane, k_{x0}, which is often parameterised using the ballooning angle $\theta_0 = k_{x0}/(k_y\hat{s})$ [5]. Here $k_y = nq/r$ is the bi-normal wavenumber and $\hat{s}$ is the magnetic shear. At finite $E \times B$ shear, modes at different θ_0 become coupled, and the effective time average growth rate of a mode becomes an average of $\gamma^{\mathrm{MTM}}(\theta_0)$; see discussion of the Floquet cycle and effective linear growth rates with flow shear in section 3.1 of [19]. The stabilising impact of $E \times B$ shear therefore is stronger when the peak in $\gamma^{\mathrm{MTM}}(\theta_0)$ is narrower and more localised. The focus of this paper is to improve our understanding of the factors determining $\gamma^{\mathrm{MTM}}(\theta_0)$ and the corresponding susceptibility of MTM turbulence to suppression through $E \times B$ shear.

[5] For a circular, high aspect ratio, low β un-shifted flux surface, θ_0 corresponds to the poloidal angle at which the mode has zero radial wavenumber.

MTMs can of course saturate via other mechanisms such as zonal fields [15, 20], local electron temperature gradient flattening [10, 21] and coupling to dissipative modes [16], though that will not be a particular focus here.

This paper also examines the applicability of recent work done by Hardman *et al* [22], where a theory is derived for electromagnetic electron-driven instabilities resembling MTMs, that have current layers localised to mode-rational surfaces and bi-normal wavelengths comparable to the ion gyroradius. The gyrokinetic equation is derived for two different regions, one inner region localised around the rational surface. Secondly an outer region far away from the rational surface at the centre of the flux tube in the local gyrokinetics simulation. In ballooning space the inner region corresponds to $\theta \gg 1$, and the outer region corresponds to $\theta \lesssim 1$. In this theory a mass ratio expansion is taken with the following ordering for β

$$\beta \sim \left(\frac{m_e}{m_i}\right)^{\frac{1}{2}} \sim k_y\rho_e \ll 1 \tag{1}$$

and an asymptotic matching condition is applied to solutions from the two regions to obtain the dispersion relation. This theory exposes an important local equilibrium parameter, β_{eff}, that increases the MTM instability drive when it is large. β_{eff} is defined as:

$$\beta_{\mathrm{eff}} = \beta_e \frac{2\pi G(\theta_0)}{\hat{s}k_y\rho_e} \tag{2}$$

where

$$G(\theta_0) = \frac{1}{qR_0}\frac{\hat{s}}{\pi}\int_{-\infty}^{\infty}\frac{B^2}{B_{\mathrm{ref}}}\frac{k_y^2}{k_\perp^2}\frac{\mathrm{d}\theta}{B.\nabla\theta} \tag{3}$$

with all the θ_0 dependence of β_{eff} being contained in $k_\perp$. $G(\theta_0)$ is highly sensitive to how $k_\perp$ varies along the field line and it is generally maximised when $\theta_0 = 0$. The integrand's θ_0 dependence is dominated by the factor $k_y^2/k_\perp^2$, and it is maximised at $k_\perp = k_y$, i.e. at $k_x = 0$. In a large aspect ratio circular geometry, $k_y^2/k_\perp^2 = (1 + \hat{s}^2(\theta - \theta_0)^2)^{-1}$, which is largest either when $\theta = \theta_0$ or when $\hat{s}$ is low. In such geometries $G(\theta_0) = 1 + \mathcal{O}(r/R)$.

A more physical picture for $G(\theta_0)$ can be built by examining the linearised form of Ampère's Law for the perturbed current and perpendicular magnetic field:

$$k_\perp^2 A_{||} = \frac{4\pi}{c}J_{||}. \tag{4}$$

MTMs generate re-connection whereby equilibrium field lines undergo a finite radial displacement over their trajectory from $\theta = -\infty \rightarrow \infty$. The radial displacement of a field line is given by:

$$\Delta\Psi = \int_{-\infty}^{\infty} \frac{k_y A_{||} \mathrm{d}\theta}{b.\nabla\theta} = \frac{4\pi}{c} \int_{-\infty}^{\infty} \frac{J_{||}}{B} \frac{B^2 k_y}{k_\perp^2} \frac{\mathrm{d}\theta}{B \cdot \nabla\theta}. \quad (5)$$

Quasi-neutrality requires a divergence-free perturbed current, $\boldsymbol{\nabla}.(J_{\|}\mathbf{b}) = 0$ resulting in:

$$B \cdot \nabla\theta \frac{\partial}{\partial\theta}\left(\frac{J_{||}}{B}\right) = 0. \quad (6)$$

Here the perpendicular current $J_\perp$ has been ordered out by the low β assumption which will ignore the ion contribution to the current. Combining equations (5) and (6) whilst dropping constants gives:

$$\Delta\Psi \propto \int_{-\infty}^{\infty} \frac{B^2}{k_\perp^2} \frac{\mathrm{d}\theta}{B \cdot \nabla\theta} \quad (7)$$

where the integrand is proportional to $G(\theta_0)$. This exposes how $G(\theta_0)$, and thus β_{eff}, represent a local equilibrium geometry parameter to which the radial field line displacement is proportional for a given perturbed parallel current $J_{\|}/B$. β_{eff} determines how efficiently a magnetic field perturbation can tap energy from the current perturbation generated by the electron temperature gradient drive, which is key in setting the MTM growth rate.

In this paper we will explore the crucial dependence of the growth rate on θ_0, which has received relatively little attention in the literature. Section 2 outlines the local equilibria and grid parameters used for gyrokinetic calculations of MTMs that will be presented for MAST and NSTX plasmas. Section 3 examines MTMs previously found in MAST [7], using both linear and nonlinear simulations. The impact of θ_0 on these modes is determined and we assess whether β_{eff} is useful as an indicator of the linear instability drive. In section 4, a similar approach is applied to an NSTX plasma [13, 14], where the MTM turbulence is found to be much more susceptible to stabilisation via $E \times B$ shear, as opposed to the MAST surface examined. This difference is explained by the impact of higher $\hat{s}$ of the NSTX plasma on the linear stability. Bicoherence analysis is used to demonstrate stronger coupling between different θ_0 in nonlinear simulations when including $E \times B$ shear providing a potential method of saturation. This all points to the importance of tailoring the safety factor profile, which is important in determining when MTMs are susceptible to sheared flow stabilisation.

2. Equilibria and numerical set up

Many different codes have been used to analyse MAST and NSTX plasmas, both linearly and nonlinearly. For the cases studied here, we use CGYRO [23].

The Miller representation [24, 25] was used to describe the local equilibrium parameters of each chosen surface from MAST and NSTX, with parameters outlined in table 1. Gradients are defined such that $a/L_X = -(a/X)\partial X/\partial r$ where a is the minor radius of the last closed flux surface. The level of $E \times B$ shear is parameterised by $\gamma_{E\times B} = -(r/q)\partial\omega_0/\partial r$, with ω_0 being the local toroidal angular rotation frequency of the plasma. All heat fluxes in this paper are normalised to $Q_{gB} = n_e T_e c_s (\rho_s/a)^2$ where $\rho_s = c_s(eB_{\mathrm{unit}}/m_D c)$, with $c_s = \sqrt{T_e/m_D}$ and $B_{\mathrm{unit}} = (q/r)\partial\psi/\partial r$.

Table 1. Local Miller parameters and reference values for the equilibrium flux surfaces simulated in this work from MAST #22 769 and NSTX #120 968, where the parameters are defined as in [24]. Here β_e is the electron plasma β normalised to $B_0 = f/R_{\mathrm{maj}}$ and $\beta_{e,\mathrm{unit}}$ utilises B_{unit} as the normalising field.

	r/a	R_{maj}/a	$\partial_r R_{\mathrm{maj}}$	a/L_n	$a/L_{T,e}$	q	$\hat{s}$
MAST	0.51	1.57	−0.13	0.22	2.11	1.08	0.34
NSTX	0.60	1.53	−0.29	−0.83	2.73	1.71	1.70
	$\gamma_{E\times B}(c_s/a)$	$\nu_{ee}(c_s/a)$	κ	s_κ	δ	s_δ	β'
MAST	0.19	0.82	1.41	0.01	0.16	0.12	−0.53
NSTX	0.18	1.45	1.71	0.11	0.13	0.17	−0.36
	$n_{\mathrm{e}}(\mathrm{m}^{-3})$	$T_{\mathrm{e}}(\mathrm{keV})$	$a(\mathrm{m})$	$B_0(\mathrm{T})$	$B_{\mathrm{unit}}(\mathrm{T})$	β_e	$\beta_{e,\mathrm{unit}}$
MAST	3.55×10^{19}	0.44	0.57	0.33	0.54	0.11	0.023
NSTX	6.01×10^{19}	0.45	0.62	0.32	0.66	0.06	0.025

This work examines ST scenarios where MTMs have been previously found. Firstly, the MAST discharge #22769 at the flux surface with $r/a = 0.51$ at $t = 0.2$ s, as discussed in [7]. This surface along with an outer flux surface close to the peak in experimental collisionality is examined in detail in [15]. Furthermore, the flux surface with $r/a = 0.6$ in the NSTX discharge #120968 at $t = 0.56$ s is examined here, which has been discussed previously in [14].

The aim of this study is to examine MTM in different regimes. Although the MTM is generally dominant in the local equilibria analysed here, different modes can become the dominant instability during parameter scans. The following choices were made to avoid mode transitions and maximise the likelihood of the MTM remaining the dominant instability. All simulations in this work were performed without $\delta B_{||}$ fluctuations and $a/L_{T,i} = 0.0$. This reduces the linear drive for other instabilities, such as KBMs and ITGs, without affecting the MTM drive [26]. This can artificially preserve MTM as the the dominant instability, making it easier to track the mode in isolation linearly. Note that the focus here is not to quantitatively predict the transport from the mode, but rather to determine the sensitivity of growth rates for particular modes to θ_0.

Linear calculations were conducted using 64 θ grid points, 8 energy grid points and 24 pitch angle points with 64 connected 2π segments. For simplicity only Lorentz collisions were included in the simulations as this was found to be sufficient for unstable MTMs. $Z_{\mathrm{eff}} = 1.0$ was used and only 2 species were simulated, electrons and deuterium. An additional filter has been used to classify a mode as an MTM by imposing a threshold level of re-connection from the perturbed radial

magnetic field by requiring the field line tearing parameter, $C_{\text{tear}} > 0.1$ where:

$$C_{\text{tear}} = \frac{|\int A_{||} \mathrm{d}l|}{\int |A_{||}| \mathrm{d}l}. \tag{8}$$

All nonlinear calculations performed here use the same initial conditions with zero zonal amplitude and a small amplitude for non-zonal modes[6].

Pyrokinetics, a python library which aims to standardise gyrokinetic analysis [27], was used to generate the input files and perform the analysis in this work.

3. MAST #22769 - Low $\hat{s}$ MTMs

MAST 22 769 - Low s MTMs Using the MAST local equilibrium parameters in table 1, from [7], the micro-stability of this equilibrium was explored as a function of $k_y\rho_s$ and θ_0, focusing on the ion scale in the bi-normal direction with simulations performed up to $k_y\rho_s = 1.1$.

3.1. Linear stability properties of the MTM

Figure 1(a) shows in blue the growth rate, γ, and mode frequency, ω, of the dominant linear instabilities at $\theta_0 = 0$. For $k_y\rho_s \leqslant 0.6$, the dominant mode is an MTM and the eigenfunction of the most unstable MTM at $k_y\rho_s = 0.5$ is illustrated in figure 1(b). This exhibits the conventional properties of an MTM in that ϕ has odd parity whilst $A_{||}$ has even parity. ϕ is significantly extended in ballooning space whilst $A_{||}$ is very narrow. This MTM is ion scale in the bi-normal direction, but these eigenfunctions illustrate its multi-scale nature in the radial direction: low k_x is needed to resolve both ϕ and $A_{||}$ in the outer layer, but very high k_x is also required to resolve ϕ in the inner layer.

An electrostatic mode becomes dominant at $k_y\rho_s > 0.6$, where the MTM becomes sub-dominant[7], and this is confirmed through an electrostatic simulation without $A_{||}$, shown in orange, where the mode frequency and growth rate are largely unchanged on removal of $A_{||}$. Furthermore, this mode is clearly unstable when $0.4 \leqslant k_y\rho_s \leqslant 0.6$, but is sub-dominant to the MTM. This mode has a frequency in the electron diamagnetic direction. It has an even parity ϕ eigenfunction and the linear fluxes indicate that it drives predominantly electron heat transport, with little ion and particle transport. It has a similar transport signature to MTM, though is definitely not an MTM given its predominantly electrostatic nature and the fact that $C_{\text{tear}} \approx 0$. Its electrostatic potential eigenfunction looks very similar to those found in [1, 22, 28, 29] for a radially localised ETG mode, and in this work is denoted as electrostatic passing electron mode (PEM).

Figure 2 illustrates a 2D scan in $k_y\rho_s$ and θ_0 that was performed to see how γ^{MTM} varies with θ_0, though this picture is somewhat complicated in the region $k_y\rho_s > 0.5$ by the PEM. The blue-yellow contours indicate the MTM growth rate where it is dominant, whilst the shaded red region at higher $k_y\rho_s$ is where the PEM is dominant. At $k_y\rho_s \leqslant 0.5$, the MTM remains the dominant mode across θ_0 and is slightly stabilised with increasing θ_0. The dependence on θ_0 is weaker as k_y is reduced. This suggests that $E \times B$ shear will have a limited impact on these modes nonlinearly. The PEM growth rate also weakly depends on θ_0 for this surface.

The $A_{||}$ eigenfunctions at $k_y\rho_s = 0.5$ are shown for $\theta_0 = 0$, 0.5π and π in figure 3(a), which is the highest $k_y\rho_s$ where the MTM is the dominant instability throughout θ_0. The peak of the eigenfunction moves away from $\theta = 0$ as θ_0 increases up to π. The periodic behaviour seen in the tails of the eigenfunction also shift with θ_0, such that when the axes are shifted by θ_0, the peaks and troughs of the eigenfunctions line up perfectly, demonstrated in figure 3(b). This indicates that the location of the peaks in the tail of the distribution function is impacted by the location of the peak around $\theta \sim 0$ and the troughs occur where $(\theta - \theta_0) \bmod 2\pi = 0$.

3.2. Validity of β_{eff} for MTMs in MAST

It is interesting to assess whether the γ^{MTM} dependence on θ_0, which decreases slightly with rising θ_0 for $k_y\rho_s > 0.4$, can be understood from a theoretical point of view. β_{eff}, defined in section 1, is calculated for this MAST case and is compared with γ^{MTM} in figure 4(a). Both monotonically decrease with θ_0, in a similar trend, supporting the suggestion from the theory that the MTM driving mechanism is less effective at lower β_{eff}.

Equation (2) shows that β_{eff} is sensitive to θ_0, β_e, k_y and $\hat{s}$, so the behaviour of the MTM can be examined whilst modifying these parameters. Figure 4(b) shows γ^{MTM} against β_{eff} for two independent scans, firstly in θ_0 (as shown in figure 4(a) and secondly in β_e (at fixed $\theta_0 = 0$) to scale β_{eff} over the same range from the θ_0 scan. These scans were performed using the MAST local equilibrium parameters with two values of $\hat{s}$: the local equilibrium value of $\hat{s} = 0.34$ shown in blue; and a higher value of $\hat{s} = 1.70$, corresponding to the value of the NSTX equilibrium discussed in section 4, indicated by the orange markers. γ^{MTM} is found to be a unique function of β_{eff} for each local equilibrium. Note, the higher $\hat{s}$ case is more unstable at a lower β_{eff}, indicating that although β_{eff} is an important parameter for MTM stability, it is not the only one.

If the critical threshold for unstable MTMs in β_e at $\theta_0 = 0$ can be determined for a given local equilibrium, this will give the critical β_{eff} for the instability. Then from geometry alone, it should be possible to assess where β_{eff} drops below this critical value as θ_0 increases, and thus determine whether the mode goes stable.

[6] The CGYRO inputs used for the initial conditions in nonlinear runs were AMP0 = 0.0 and AMP = 0.001.

[7] This differs from results reported in [15] for the same local equilibrium, where no overlap of modes was seen. This is due to a difference in the collision operators used. [15] used a Sugama operator with more physics, whilst for simplicity a Lorentz operator was chosen here.

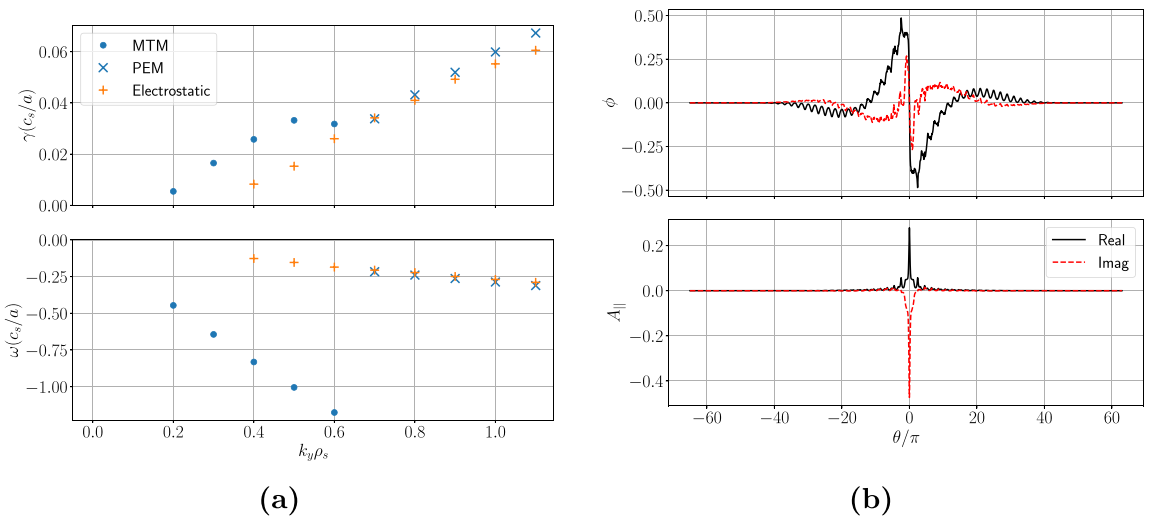

Figure 1. (*a*) Eigenvalues for the MAST local equilibrium at $\theta_0 = 0$, with the dominant instability of an electromagnetic simulation shown in blue and an electrostatic simulation shown in orange. The dots illustrate a MTM and the crosses a passing electron mode (PEM). (*b*) ϕ and $A_{||}$ eigenfunctions of the MTM at $k_y\rho_s = 0.5$.

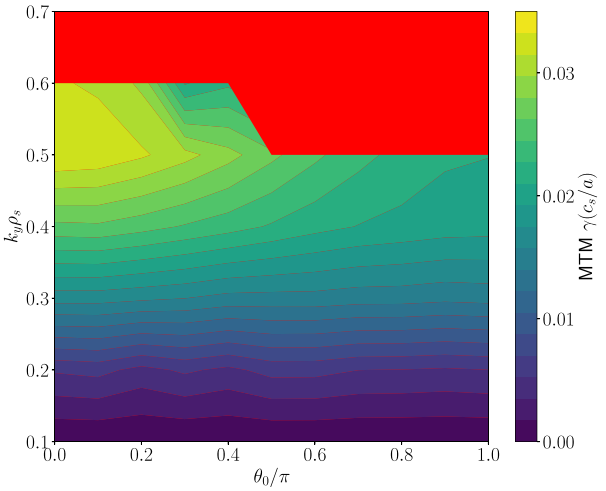

Figure 2. A 2D contour plot showing the growth rate γ of MTMs (where they dominate) for the MAST local equilibrium, plotted against θ_0 and $k_y\rho_s$. The blue-yellow contours denote the MTM growth rate, whilst the shaded red region shows where the PEM is dominant. The modes were differentiated using the field line tearing parameter C_{tear}.

In this MAST equilibrium, the weak dependence of γ^{MTM} (and β_{eff}) on θ_0 suggests that MTMs should only be very weakly impacted by equilibrium $E \times B$ shear.

3.3. Impact of $E \times B$ shear on nonlinear MAST simulations

Nonlinear simulations were performed to assess the impact of $E \times B$ shear on MTM turbulence in this MAST equilibrium. These simulations required 384 k_x grid points with $k_{x,\min}\rho_s = 0.019$ and 24 k_y grid points with $k_{y,\min}\rho_s = 0.035$. The spectral wavenumber advection method was used to implement flow shear [30]. A resolution scan is outlined in appendix confirming convergence. Without any imposed $E \times B$ shear, ion scale k_y simulations of the MAST equilibrium saturate at a small level of flux, which is well below the experimental level[8]. The simulation shown in figure 5 has a predicted electron flux of $Q_e = (2.6 \pm 0.3) \times 10^{-1} Q_{gB}$, calculated by taking the mean value in the latter third of the simulation with the uncertainty given by the standard deviation. This dominates compared to the particle and ion heat flux which are $\Gamma_e = (3.0 \pm 0.3) \times 10^{-3} \Gamma_{gB}$ and $Q_i = (5.9 \pm 0.4) \times 10^{-3} Q_{gB}$ respectively. Furthermore, the transport is dominated by the electromagnetic contribution, with a time averaged $Q_e^{A_{||}}/Q_{\text{total}} = 0.87$, indicating that it is indeed the MTM that is causing this transport, rather than the PEM This is further confirmed by running this case electrostatically, which results in transport three orders of magnitude smaller. These simulations saturate with large zonal ϕ and $A_{||}$ which may be relevant to the saturation mechanism. Contour plots of ϕ and $A_{||}$ for the case without $E \times B$ shear demonstrate this in figure 6. Recent work by Giacomin *et al* [15], which also examined this equilibrium, suggests that the stochastic transport, which is typically the dominant channel for MTMs, is weak in this region due to low magnetic shear resulting in a large separation between rational surfaces compared to the island width. A simulation was then performed adding in the experimental level of $E \times B$ shear with $\gamma^{\text{exp}}_{E\times B} = 0.19 c_s/a$. The heat flux here is $Q_e = (2.4 \pm 0.5) \times 10^{-1} Q_{gB}$, which is similar to the case without $E \times B$ shear. The impact of equilibrium $E \times B$ shear on MTM turbulence is minimal, consistent with expectations from the weak dependence of γ^{MTM} on θ_0, as discussed in section 3.1.

The level of stochasticization can be visualised in this case using a Poincaré map of the magnetic field line, where the perturbed magnetic field line is followed for many toroidal turns

[8] This equilibrium also contained electron scale ETG modes which contributed significantly more heat flux much closer to the experimental level, suggesting that the MTMs were not as experimentally relevant in the chosen radial position [15].

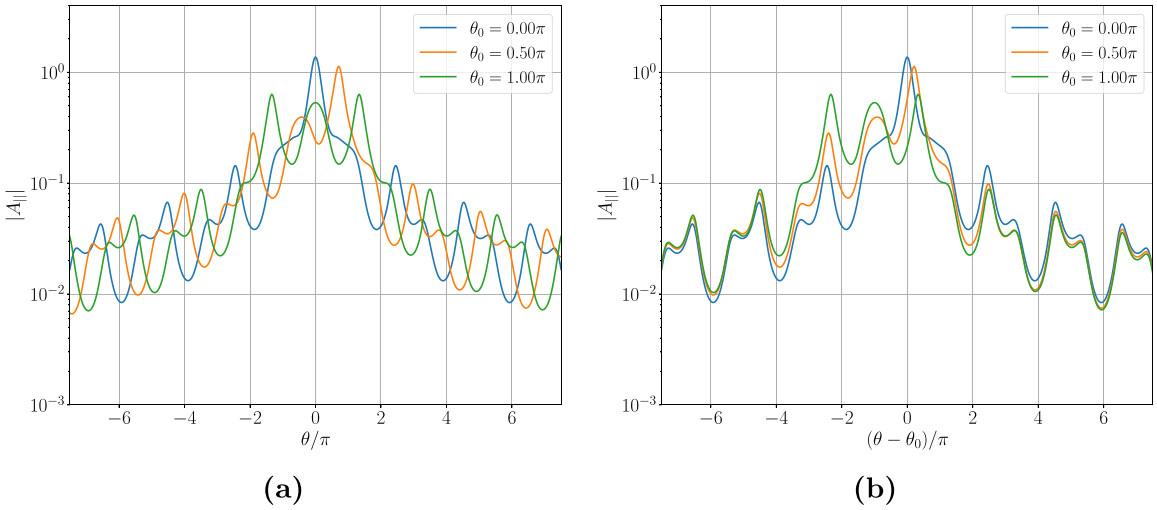

Figure 3. The eigenfunction of the MTM in MAST at $k_y\rho_s = 0.5$ at various different θ_0. (a) plots against the θ, whilst (b) shifts the eigenfunctions by θ_0. Doing so lines up the eigenfunction when $|\theta| > \pi$.

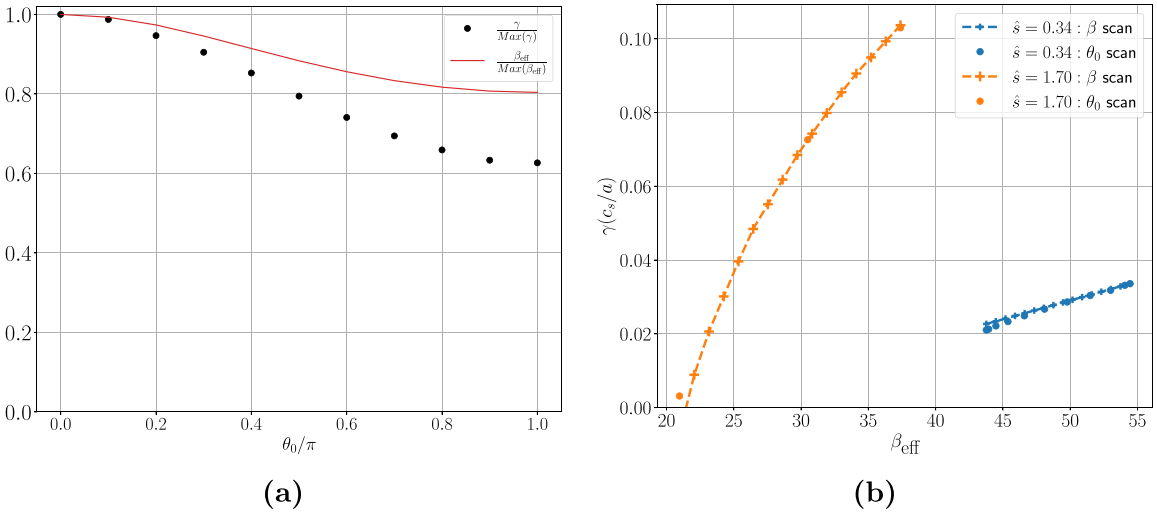

Figure 4. (a) The growth rate (black) and β_{eff} (red) normalised to their respective maxima for the MAST MTM at $k_y\rho_s = 0.5$ against θ_0. (b) A β_{eff} scan via changing β_e (dashed lines) and θ_0 (dots). This was done at the equilibrium $\hat{s} = 0.34$ (blue) and at the NSTX value of $\hat{s} = 1.70$ (orange).

around the flux surface. Figure 7 shows the Poincaré plot for these nonlinear MAST simulations, where the colour denotes the starting radial position of the field line. The development of magnetic islands is clearly shown. When including $E \times B$ shear, magnetic islands form but with slightly less overlap reducing the level of stochasticization.

4. NSTX #120968 - High $\hat{s}$ MTMs

Here we assess whether β_{eff} is also a reliable indicator of linear MTM stability for the local equilibrium from NSTX with the local parameters in table 1, taken from [8], where MTMs were also found. As with the MAST case, we assess the dependence of γ^{MTM} on θ_0, and the impact of $E \times B$ shear on the saturation level of the turbulence in nonlinear simulations.

4.1. Linear stability properties of the MTM

Figure 8(a) shows the growth rate and mode frequency for the MTMs found in NSTX. The results here match well with that shown in [13], with no electrostatic mode being seen here. Compared to MAST, the MTMs here have a much larger normalised growth rate so it is not surprising that they are unstable up to a higher $k_y\rho_s = 1.5$. It might also be expected that any nonlinear simulation without sheared flow would saturate at a higher flux than for MAST. The eigenfunctions at $k_y\rho_s = 0.5$ are shown in figure 8(b); the electrostatic potential is considerably less extended in ballooning space compared to figure 1(b), due to both the higher collisionality and higher $\hat{s}$.

A 2D linear stability scan has been performed in k_y and θ_0, similar to that performed in section 3, spanning $k_y\rho_s$ from $0.1 \rightarrow 1.1$ and θ_0 from $0 \rightarrow 2\pi$. Figure 9 presents a contour plot of the MTM growth rate, where the white line shows

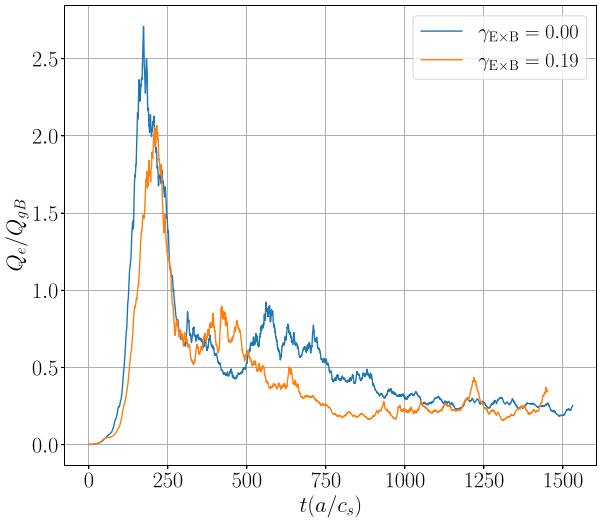

Figure 5. Nonlinear electron heat flux prediction for the MAST case when $\gamma_{E\times B} = 0.0$ (blue) and $\gamma_{E\times B} = 0.19 c_s/a$ (orange). Note that the electromagnetic electron heat flux dominates the total flux driving >87% of the total heat transport in both of these simulations. The vertical dashed line denotes the time from which the average and uncertainty in the flux is calculated. The particle and the ion heat fluxes are two orders of magnitude smaller compared to the electron heat flux.

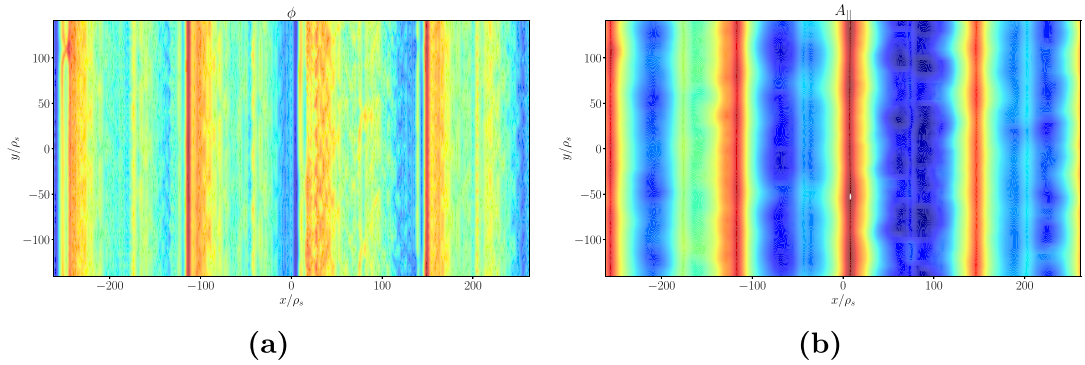

Figure 6. Contour plots of (*a*) ϕ and (*b*) $A_{||}$ at $\theta = 0$ at the final time slice for the MAST simulation without $E \times B$ shear showing large zonal amplitudes in both fields.

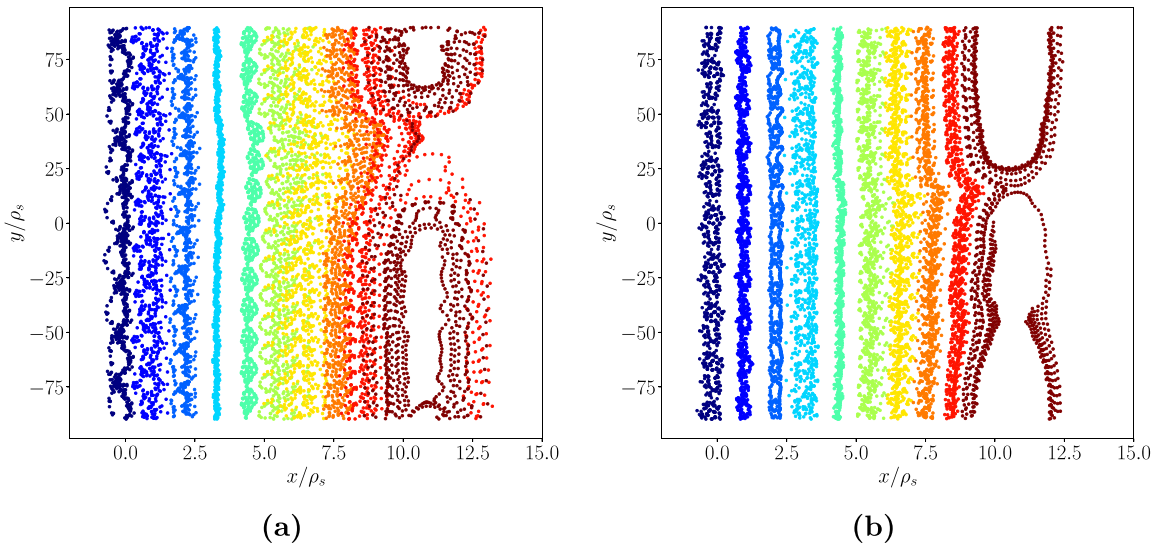

Figure 7. Poincaré plots for the MAST nonlinear simulation (*a*) without $E \times B$ shear and (*b*) with $E \times B$ shear. The colour denotes the starting radial position of the field line. Magnetic islands are formed in both cases but there is weak island overlap.

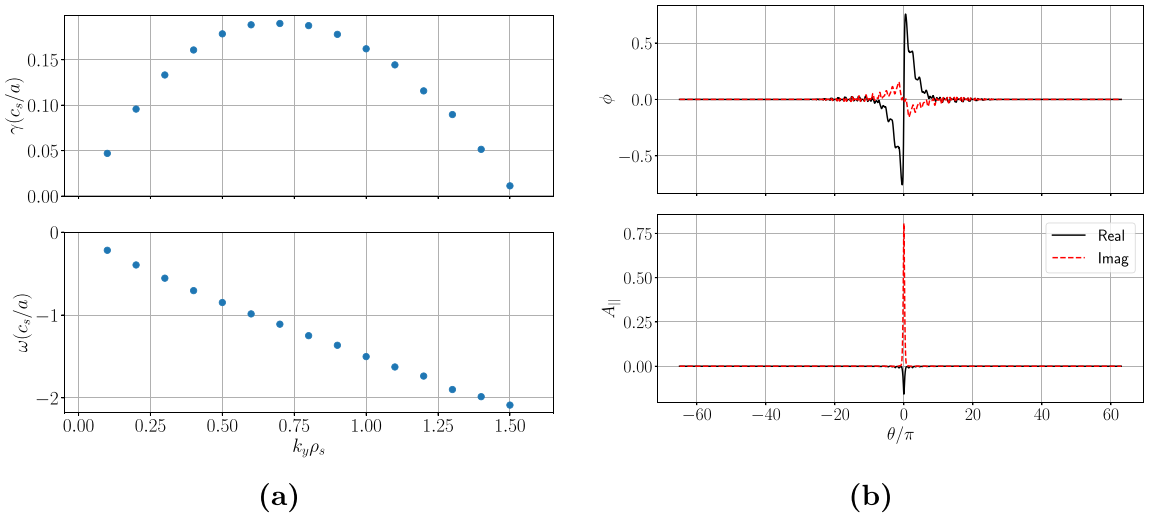

Figure 8. (a) Eigenvalues of the NSTX equilibrium at $\theta_0 = 0$. (b) Eigenfunction of MTM at $k_y\rho_s = 0.5$ in the NSTX equilibrium.

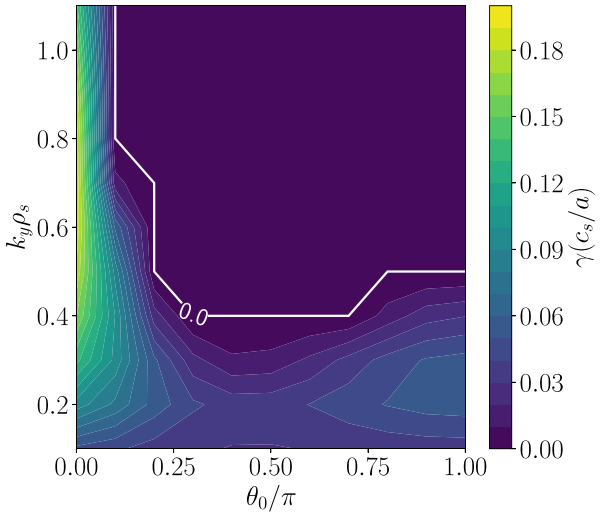

Figure 9. 2D contour plot of the growth rate against θ_0 and $k_y\rho_s$ for the NSTX local equilibrium. The solid white line denotes the marginal stability contour.

the marginal stability contour. The only unstable mode found here was the MTM. For $k_y\rho_s \leqslant 0.3$, the mode remains unstable for all values of θ_0, but the growth rates are non-monotonic with θ_0. At $k_y\rho_s = 0.4$ a window of stability appears centred around $\theta_0 = 0.4\pi$, getting wider in θ_0 at higher k_y, restricting the unstable space to a narrow region around $\theta_0 = 0.0$.

4.2. Impact of magnetic shear on the MTMs stability

The MAST and NSTX local equilibria show a very different dependence of γ^{MTM} on θ_0, even though the values of many local parameters are quite similar. We have identified the local equilibrium parameters responsible for this striking difference by individually changing each equilibrium parameter from NSTX to that from MAST. This highlighted the magnetic shear, $\hat{s}$, as the most significant parameter. Figure 10(a) shows how the growth rate varies with θ_0 for $k_y\rho_s = 0.5$ using the NSTX equilibrium at two different values of $\hat{s}$. The orange line uses the NSTX equilibrium value of $\hat{s} = 1.70$ and the MAST value of $\hat{s} = 0.34$ is in blue. With the NSTX equilibrium $\hat{s}$, the mode is stable for $\theta_0 > 0.1\pi$, which coincides with β_{eff} dropping below 10. At the lower MAST value of $\hat{s}$ the mode is unstable and $\beta_{\mathrm{eff}} > 50$ across the whole range in θ_0.

To further confirm the impact of $\hat{s}$, simulations were run for the MAST local equilibrium case in section 3 with the equilibrium MAST $\hat{s}$ in blue and the higher NSTX $\hat{s}$ in orange, with the results shown in figure 10(b). At higher $\hat{s}$, γ^{MTM} becomes much more sensitive to θ_0 and becomes stable at higher θ_0. (Note the electrostatic PEM at $k_y\rho_s = 0.5$ found in the MAST local equilibrium is stabilised with higher $\hat{s}$.) This suggests that MTMs found in regions with high magnetic shear may have their transport suppressed by $E \times B$ shear. Figure 11 show 2D contour plots of γ^{MTM} against θ_0 and $\hat{s}$ for the MTM at $k_y\rho_s = 0.3$ in NSTX and for the MTM at $k_y\rho_s = 0.5$ in MAST, where it is clear that the dependence of γ^{MTM} on θ_0 is increasingly insensitive and monotonic at low values of $\hat{s}$, and that the unstable region with peak growth rate at $\theta_0 = 0$ narrows as $\hat{s}$ is increased. All the unstable modes found in these scans were MTMs.

As mentioned earlier, increasing $\hat{s}$ will make β_{eff} drop off faster with θ_0, which according to the model will help to stabilise the mode. Figure 10 shows that β_{eff} has a stronger dependence on θ_0 at higher $\hat{s}$, dropping below 10 by $\theta_0 = 0.3\pi$ for both equilibria. Note the higher $\hat{s}$ cases have a lower β_{eff} but are more unstable at $\theta_0 = \pi$. This is not inconsistent with the theory as $\beta_{e,\mathrm{crit}}$ will also change with $\hat{s}$. If this can be determined independently by a reduced model then it will be possible to determine at what θ_0 the mode goes stable, which was shown in figure 4(b). The change in β_{eff} can be attributed to how $k_\perp$ increases along the field line in the two different equilibria as the larger NSTX $\hat{s}$ will result in $k_\perp$ becoming proportionally larger for a given ballooning angle.

Magnetic shear only appears within the definitions of k_x, $k_\perp$, the curvature drift and the grad-B drift terms within gyrokinetic equation. To isolate which of one the impacts of

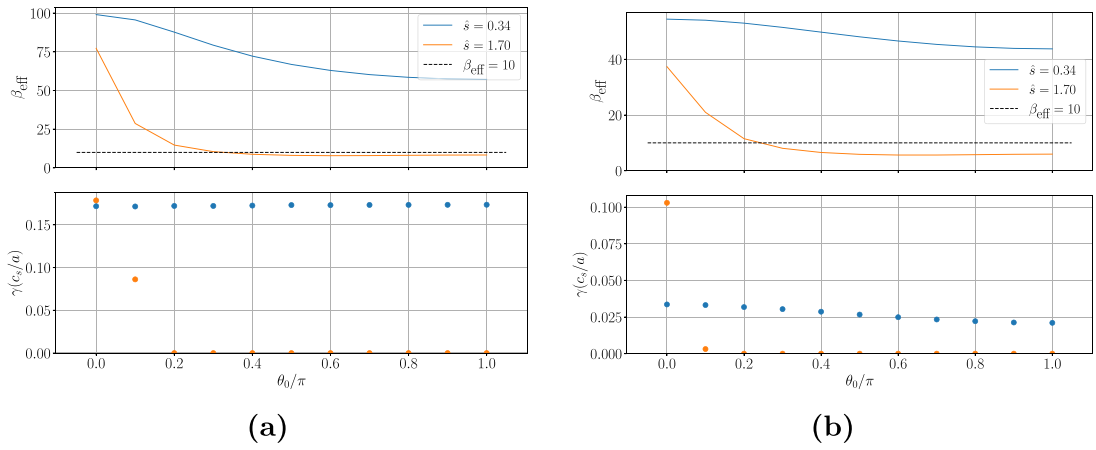

Figure 10. Comparing how β_{eff} (top) and γ (bottom) change with θ_0 for $k_y\rho_s = 0.5$. (*a*) and (*b*) use the NSTX and MAST equilibria respectively. In both figures, simulations using the MAST $\hat{s} = 0.34$ are shown in blue and the NSTX $\hat{s} = 1.70$ are in orange. The black dashed line illustrates $\beta_{\text{eff}} = 10$.

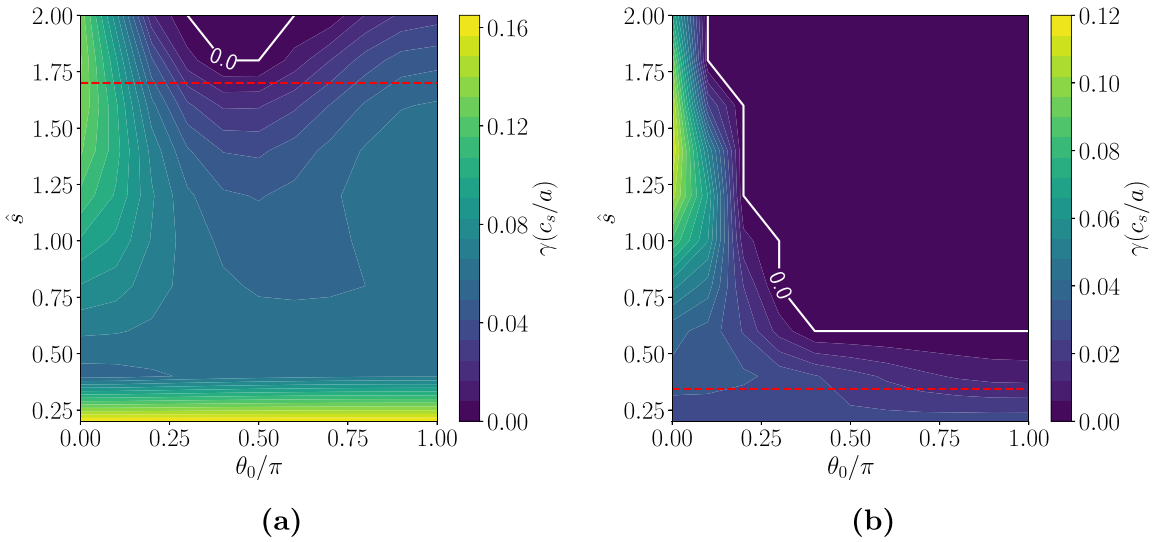

Figure 11. 2D contour plot of the growth rate against θ_0 and $\hat{s}$ for (*a*) the NSTX equilibrium at $k_y\rho_s = 0.3$ and (*b*) the MAST equilibrium at $k_y\rho_s = 0.5$. The dashed red line denotes the equilibrium $\hat{s}$ for that surface.

changing $\hat{s}$ is responsible for the changes in the stability, several NSTX simulations were performed where $\hat{s}$ was artificially lowered to the MAST value independently in each place in the gyrokinetic equation where it appears. This revealed that the impact of $\hat{s}$ on $k_\perp$ is entirely the responsible for γ^{MTM} becoming insensitive to θ_0 at low $\hat{s}$. In a more detailed refinement of this investigation focusing on the impact of magnetic shear on $k_\perp$, the change in the dependence of γ^{MTM} on θ_0, illustrated in figure 12, can be attributed directly to where $k_\perp$ enters Ampère's law[9], Modifying $k_\perp\rho_s$ in the NSTX local equilibrium to use the lower $\hat{s}$ value from MAST, the growth rate actually increases with θ_0 (which is also found in high q MAST simulations that will be shown later in figure 14(*b*)). This confirms that it is specifically how high magnetic shear impacts Ampère's law that allows θ_0 stabilisation and thus for $E \times B$ shear suppression to be effective. This provides further evidence that β_{eff} is a relevant parameter.

[9] $\delta\mathbf{B}_\perp \propto 1/k_\perp$ from equation (4), so the perturbed field is increasingly localised in the parallel direction at higher $\hat{s}$ because $k_\perp$ increases more rapidly with θ.

4.3. *Validity of β_{eff} for MTMs in NSTX*

The parameter β_{eff} is inversely proportional to k_y which also helps explain why the MTM has a narrowing window of stability in θ_0 (centred around $\theta_0 = 0.0$) at higher k_y. For the original NSTX case, β_{eff} is shown for 3 different $k_y\rho_s$ in figure 13, and at higher $k_y\rho_s$, β_{eff} is lowered. However, $k_y\rho_s = 0.7$ has the lowest β_{eff} at $\theta_0 = 0.0$, but is the most unstable out of the 3 $k_y\rho_s$ examined here. This indicates, unsurprisingly, that the linear growth rate is influenced by other parameters in addition to β_{eff}, as are included in the parameter dependence derived in [22].

However, this theory is not able to explain the behaviour at the lowest $k_y\rho_s$ where the growth rate is non-monotonic with

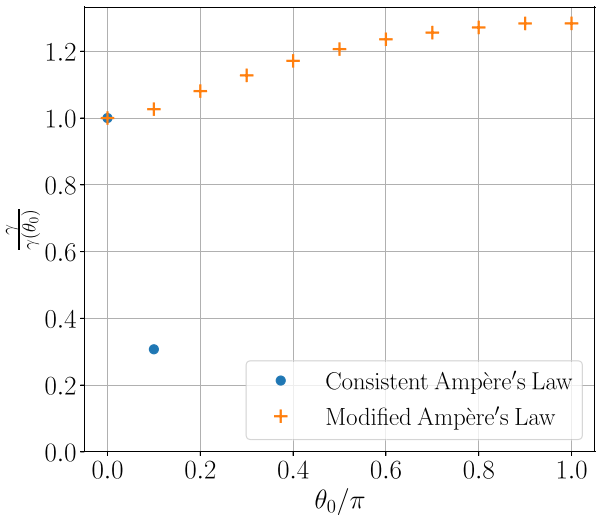

Figure 12. Growth rate of the MTM at $k_y\rho_s = 0.6$ for NSTX equilibrium using the consistent $k_\perp\rho_s$ in Ampère's law (blue) and the modified Ampère's law using $k_\perp\rho_s$ with an artificially lower $\hat{s}$ (orange).

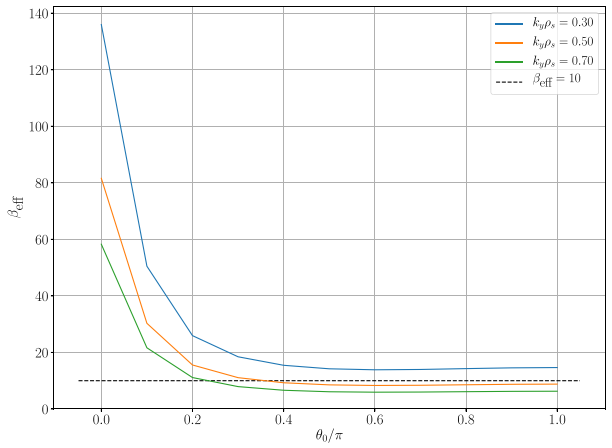

Figure 13. $\beta_{\rm eff}$ as a function of θ_0 at different $k_y\rho_s$ for the NSTX equilibrium. The black dashed line illustrates $\beta_{\rm eff} = 10$.

θ_0. For instance, in figure 13 at $k_y\rho_s = 0.3$, $\beta_{\rm eff}$ is slightly non-monotonic with θ_0, but not enough to explain the large growth rate found at $\theta_0 = \pi$. This was different in the MAST equilibrium, where both $\gamma^{\rm MTM}$ and $\beta_{\rm eff}$ had a consistent monotonic dependence on θ_0. In order to try to understand this, a scan in q was performed for the NSTX local equilibrium. Figure 14(a) shows a contour plot of $\gamma^{\rm MTM}(k_y\rho_s = 0.3, \hat{s} = 1.70)$ as a function of q and θ_0. In this scan MTMs are only unstable at $\theta_0 = \pi$ when $q > 1.2$. Whilst at lower q, $\gamma^{\rm MTM}$ decays monotonically with θ_0, and there is no instability at $\theta_0 = \pi$[10]. Furthermore, figure 14(b) shows a similar 2D scan for the MAST equilibrium where there is a relatively flat dependence of $\gamma^{\rm MTM}(k_y\rho_s = 0.5, \hat{s} = 0.34)$ on θ_0 at low q, which becomes slightly peaked at $\theta_0 = \pi$ at higher q.

[10] All modes in figure 14(a) satisfy the MTM criterion $C_{\rm tear} > 0.1$.

The peaking of $\gamma^{\rm MTM}$ at $\theta_0 = \pi$, found in the above gyrokinetics simulations at higher q, is not captured in Hardman's model [22]. This is likely due to its low β ordering assumptions, and in particular its neglect of the perturbed perpendicular current $J_\perp$, breaking down at higher q. In the model, $J_\perp$ is excluded in the charge continuity equation, as shown in equation (6). However, the ratio of $(\nabla\cdot J_\perp)/(\nabla\cdot J_{||}) \propto \beta(qR/a)^2$, so increasing these terms makes $J_\perp$ term larger which violates this ordering. This indicates that changes to β or $(R/a)^2$ should have a similar impact to changes in q^2.

To test this, two additional sets of scans were performed changing β and R/a shown in figures 15 and 16 respectively. For both parameters, scans were performed in two ways. Firstly whilst maintaining a fixed $\beta(qR/a)^2$, would maintain the relative size of $J_\perp$. Here we see in both figures 15(a) and (b) that $\gamma^{\rm MTM}$ remains non-monotonic throughout, contradicting the model as expected. Secondly, scans were performed whilst allowing $\beta(qR/a)^2$ to change, shown in figures 15(b) and (c), which modifies the size of $J_\perp$ in a similar manner to the previous q scan. Here the model's prediction is recovered as $\beta(qR/a)^2$ is reduced, similar to the lowering of q, which provides further evidence that the NSTX equilibrium is pushing beyond the orderings of the model.

4.4. Impact of $E\times B$ shear on nonlinear NSTX simulations

Figure 9 shows that a large region of the $(k_y\rho_s, \theta_0)$ phase-space is stable in the reference equilibrium of NSTX, suggesting that $E\times B$ shear may help suppress the MTM transport. Nonlinear simulations used 256 k_x grid points with a $k_{x,\rm min}\rho_s = 0.068$ and 12 k_y grid points with $k_{y,\rm min}\rho_s = 0.07$ to perform a scan in $\gamma_{E\times B}$, with the experimental value $\gamma^{\rm exp}_{E\times B} = 0.18c_s/a$. A resolution scan is outlined in appendix confirming convergence. Figure 17 shows the level of electron heat flux for 3 different nonlinear simulations. When $\gamma_{E\times B} = 0.0$, the simulation was found to saturate around $Q_e = (32\pm3)Q_{gB}$[11]; This is significantly higher than the MAST case and can be attributed to the higher MTM growth rates, together with a higher q and $\hat{s}$, reducing the separation between adjacent rational surfaces and enhancing electron heat transport from stochastic magnetic fields [15, 31]. At $\gamma_{E\times B} = 0.5\gamma^{\rm exp}_{E\times B} = 0.09c_s/a$, the simulation was found to saturate at $Q_e = (4\pm1)Q_{gB}$, which is within the error of the experimental turbulent heat flux, shown in the shaded grey area. With the full $\gamma_{E\times B} = \gamma^{\rm exp}_{E\times B} = 0.18c_s/a$, fluxes drop even further to $Q_e = (2.3\pm0.4)Q_{gB}$, slightly below the experimental value, though this likely lies within the uncertainty of $\gamma^{\rm exp}_{E\times B}$[12]. The nonlinear simulations of

[11] Note that the same simulation was previously found to not saturate in [26]. Here numerical instabilities that were responsible have been avoided through a recent improvement to the CGYRO parallel dissipation scheme—git commit 903307e.

[12] We note that these CGYRO simulations are arguably more consistent with NSTX data than previously published MTM simulations using GYRO, where including $E\times B$ shear resulted in $Q_e \ll Q^{\rm exp}_e$ [14] and the experimental heat flux could only be matched if $E\times B$ was neglected.

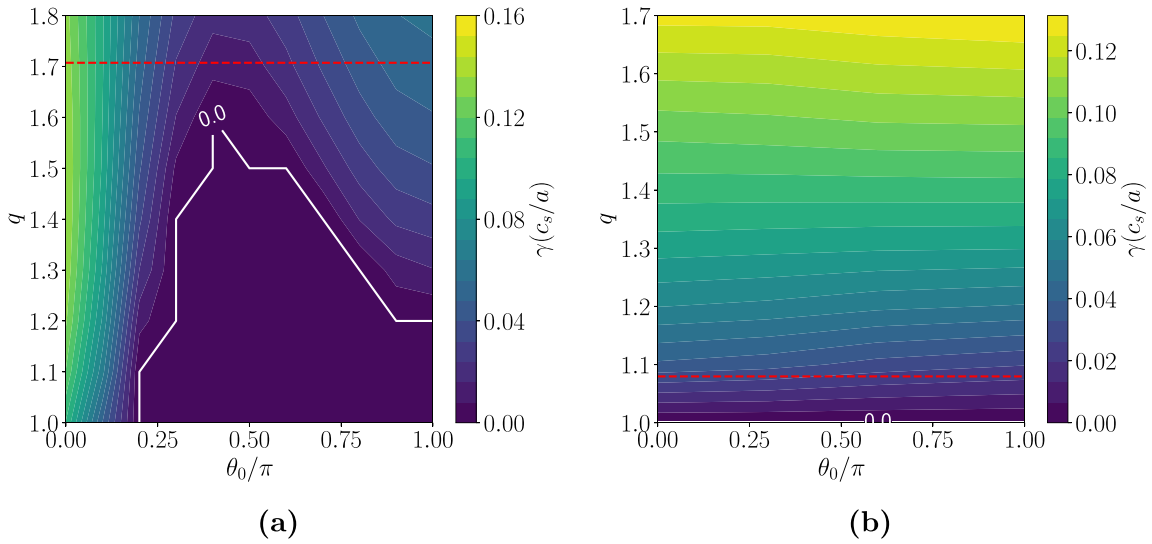

Figure 14. 2D contour plot of the growth rate against θ_0 and q for (a) the NSTX equilibrium at $k_y\rho_s = 0.3$ which has $\hat{s} = 1.70$ and (b) the MAST equilibrium at $k_y\rho_s = 0.5$ which has $\hat{s} = 0.34$. The dashed red line denotes the equilibrium q for that simulation.

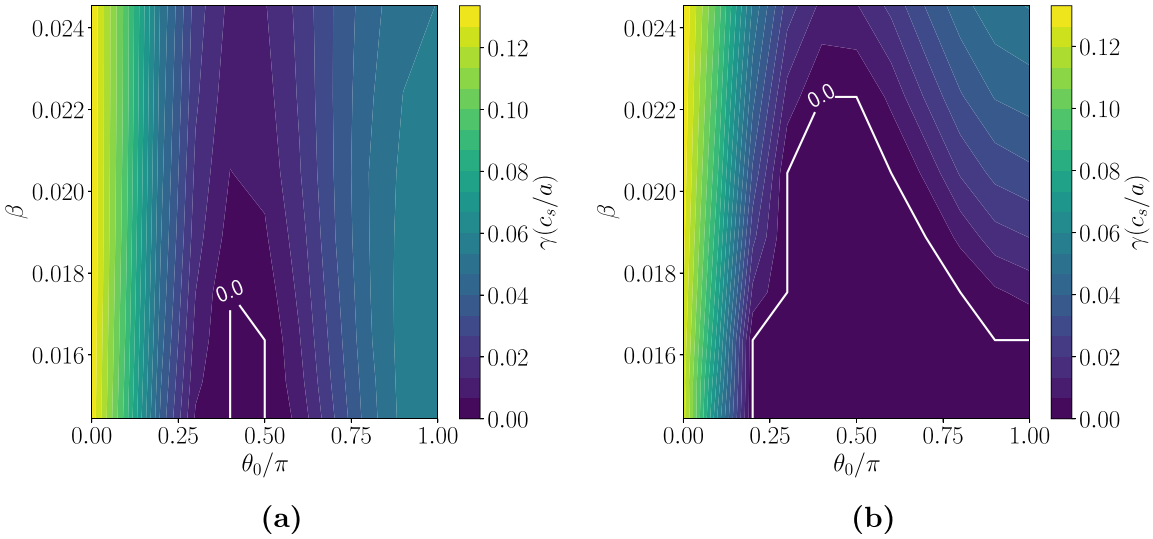

Figure 15. 2D contour plot of the growth rate for the NSTX equilibrium against θ_0 when (a) changing β whilst fixing $\beta(qR/a)^2$ by adjusting R/a and (b) changing β at fixed $(qR/a)^2$.

figure 17(a) demonstrate that when γ^{MTM} has a strong dependence on θ_0, $E \times B$ shear can be effective in suppressing MTM transport; in this NSTX case the electron heat flux reduces by more than an order of magnitude. Figure 17(b) examines the amplitude of $\Sigma_{kx}|A_{||}(\theta = 0, k_y\rho_s = 0.07)|$ for these three simulations and it is clear that the amplitude of this mode oscillates when $E \times B$ shear is included with the frequency of the oscillation being proportional to the level of $E \times B$ shear further indicating that coupling to stable modes is occurring.

The level of stochasticization is shown for the nonlinear NSTX simulations via Poincaré plots in figure 18. It is clear that when compared to the MAST simulations in figure 7 there is significantly more stochasticization which is due greater island overlap at higher $\hat{s}$ [15]. Moreover these plots demonstrate including $E \times B$ shear reduces the level of stochasticization with significantly lower radial variation.

Note that the suppression of MTM turbulence was not observed in the nonlinear simulations of figure 5, for the MAST surface at lower $\hat{s}$ where γ^{MTM} is insensitive to θ_0. Even without flow shear, however, the absolute fluxes are extremely modest on this MAST surface due to the increased distance between rational surfaces at lower $\hat{s}$ [15]. Figure 19(a) shows a nonlinear simulation for the NSTX surface, but using the lower value of $\hat{s} = 0.34$ taken from the MAST surface: it is clear that the impact of $E \times B$ shear is also minimal here. Similarly, a nonlinear MAST simulation was performed with the higher value of $\hat{s} = 1.70$, shown in figure 19(b) where the $E \times B$ shear reduces the heat flux significantly. Thus we can conclude that

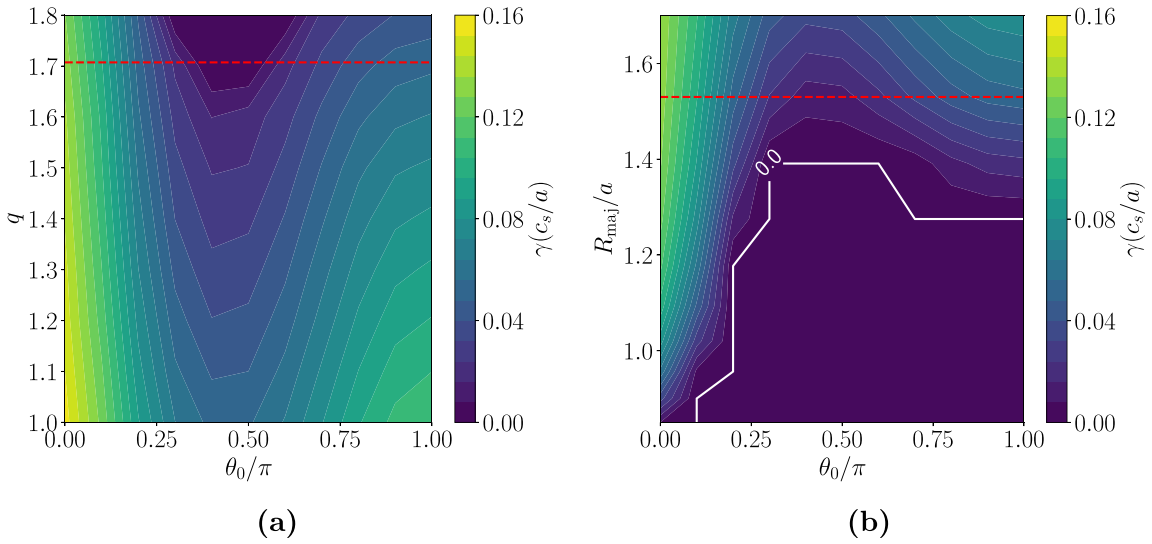

Figure 16. 2D contour plot of the growth rate for the NSTX equilibrium against θ_0 when (a) changing q whilst fixing $\beta(qR/a)^2$ by adjusting R/a and (b) changing R/a at fixed βq^2. The dashed red line denotes the equilibrium value for that simulation.

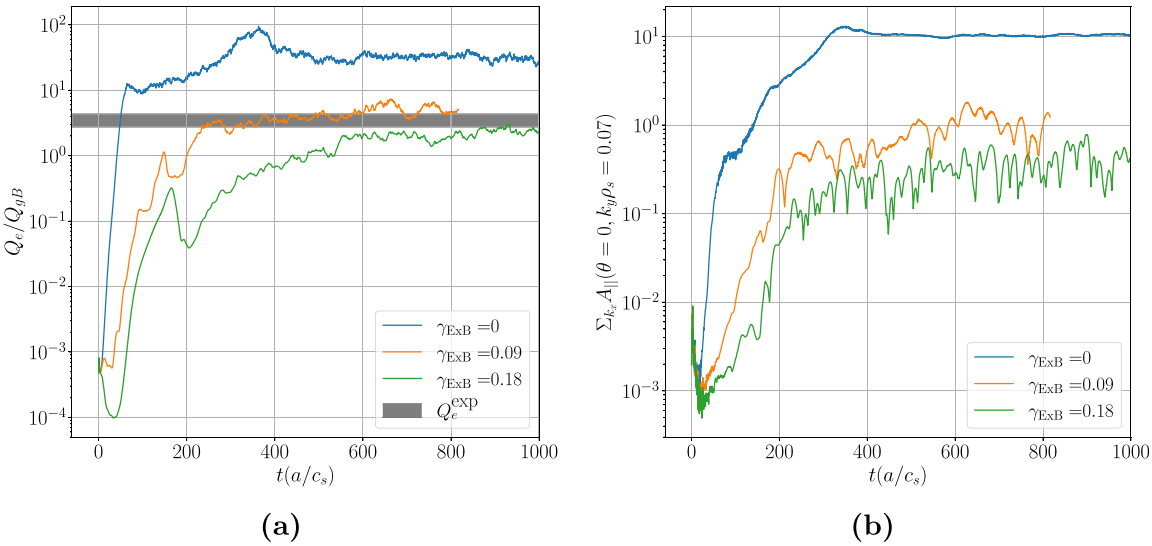

Figure 17. Nonlinear NSTX simulations with varying levels of $E\times B$ shear showing (a) the electron heat flux and (b) $\Sigma_{kx}|A_{||}(\theta=0,k_y\rho_s=0.07)|$. Here $\gamma^{\mathrm{exp}}_{E\times B}=0.18c_s/a$. Note that the electron heat flux dominated the total flux driving $>96\%$ of the total heat transport in these simulations. The grey band in (a) denotes the experimentally measured anomalous heat flux. The average and uncertainty in the flux is calculated from the final 50% of time from each simulation.

$E\times B$ shear suppression of MTM turbulence is more effective when γ^{MTM} is more strongly ballooning, which is favoured at higher $\hat{s}$.

4.5. Demonstration of mode coupling via bicoherence analysis

Bicoherence is an analysis method that determines the level of triadic mode coupling by examining whether three modes remain phase locked throughout statistically equivalent periods of a simulation. Given that there are two different wavenumbers, it is necessary to determine the 2D bicoherence. The 2D bicoherence square for a complex field X is given by

$$b^2(X)=\frac{|B(k_{x1},k_{y1},k_{x2},k_{y2})|^2}{\langle|X(k_{x1},k_{y1})X(k_{x2},k_{y2})|\rangle^2\langle|X(k_{x3},k_{y3})|\rangle^2} \tag{9}$$

where B, the bispectrum is given by

$$B(k_{x1},k_{y1},k_{x2},k_{y2})=\langle X(k_{x1},k_{y1})X(k_{x2},k_{y2})\overline{X(k_{x3},k_{y3})}\rangle \tag{10}$$

with $k_{x3}=k_{x1}+k_{x2}$, $k_{y3}=k_{y1}+k_{y2}$, $\overline{X}$ denotes the complex conjugate of X, and $\langle\rangle$ denotes an average over many realisations. If the modes at (k_{x1},k_{y1}), (k_{x2},k_{y2}) and (k_{x3},k_{y3}) are

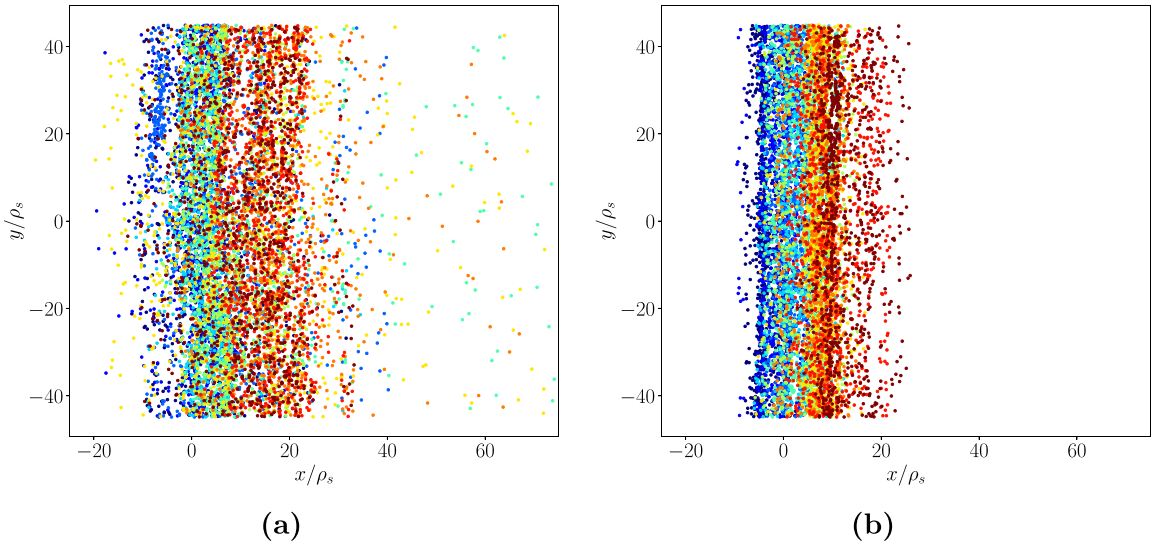

Figure 18. Poincaré plots for the NSTX nonlinear simulation (*a*) without $E \times B$ shear and (*b*) with $E \times B$ shear. The case with $E \times B$ shear has significantly less stochasticization which corresponds to lower heat fluxes.

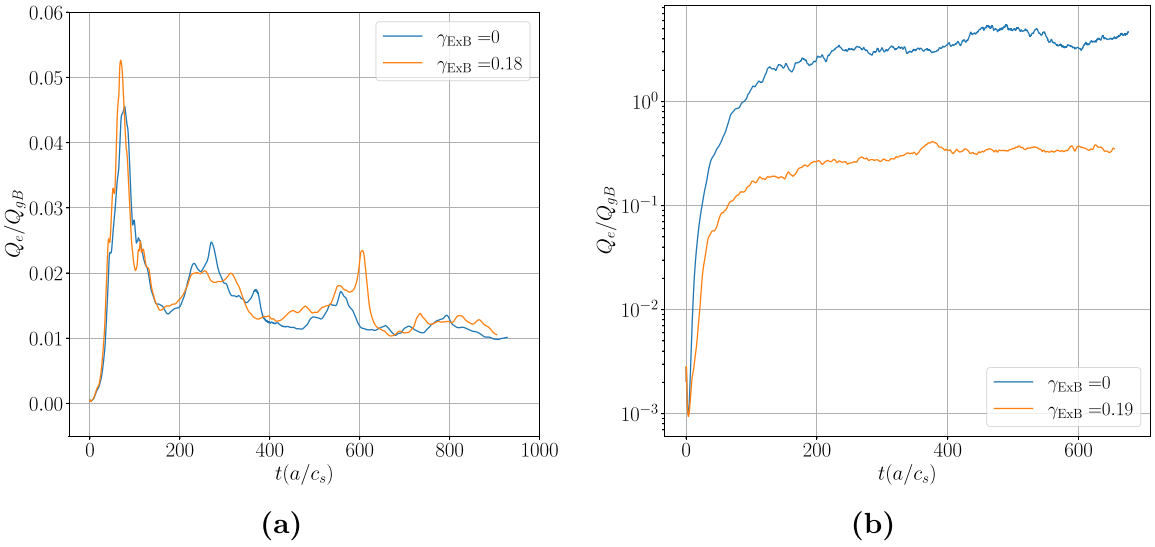

Figure 19. Nonlinear electron heat flux for simulations of (*a*) NSTX with a lower $\hat{s} = 0.34$ and varying levels of $E \times B$ shear which has little effect. (*b*) MAST with a higher $\hat{s} = 1.70$ and varying levels of $E \times B$ shear which has a significant effect. Note that the electron heat flux dominated the totallux driving $> 92\%$ of the total heat transport in these simulations.

not coupled then their complex triple product will have random phases so will average to zero over many realisations, but if there is strong coupling then this average will have a non-zero value. The normalised bicoherence, b^2, runs between 0 (no phase coupling) and 1 (entirely phase coupled). It should be noted that bicoherence cannot determine the direction of energy transfer but only if modes are coupled [32].

Given that $A_{||}$ is the dominant field with MTMs, the bicoherence square of $A_{||}(\theta = 0)$ is examined for the NSTX case with and without $E \times B$ shear where the average is taken over many time slices. The bicoherence square is calculated for two different time periods within the simulation, firstly in the linear phase and secondly in the saturated state for the final $200a/c_s$ of the simulations.

For non-stationary periods, such as the linear phase, taking the bicoherence of $A_{||}$ would not be valid given that its amplitude is exponentially increasing. To remove this effect it is necessary to examine phases directly $\hat{A}_{||} = A_{||}/|A_{||}|$. We expect that cases with $E \times B$ will have significantly more mode coupling between different θ_0 which corresponds to coupling between different $k_x\rho_s$ modes in nonlinear simulations.

Figure 20 shows the normalised bicoherence, b^2, for $\hat{A}_{||}(\theta = 0)$ between a fixed zonal mode, $(k_{x1}\rho_s = 0.14, k_{y1}\rho_s = 0.0)$ and a range of non-zonal finite $k_y\rho_s$ modes during the linear phase of the simulation, where the horizontal and vertical axes correspond to $k_{x2}\rho_s$ and $k_{y2}\rho_s$ respectively. The tertiary mode, $(k_{x3}\rho_s, k_{y3}\rho_s)$, here corresponds to mode coupling at the same non-zero $k_y\rho_s$ but shifted along in $k_x\rho_s$. For the case

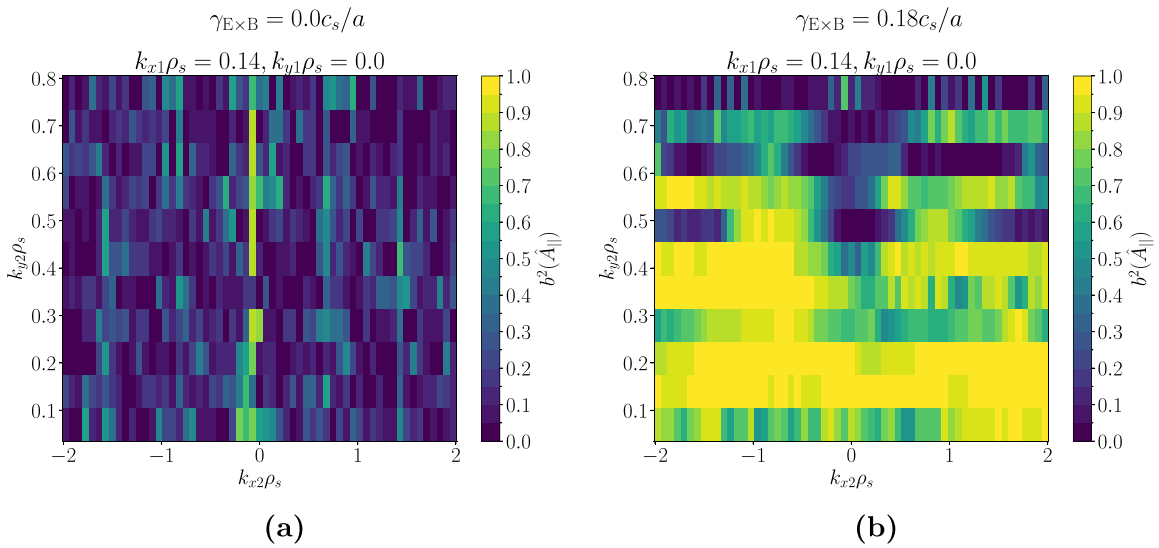

Figure 20. Normalised bicoherence square, b^2, evaluated using $A_\parallel(\theta = 0)$ in the linear phase of the NSTX nonlinear simulation (a) when $\gamma_{E\times B} = 0$, and (b) when $\gamma_{E\times B} = 0.18 c_s/a$. The bicoherence is between a purely zonal mode ($k_{x1}\rho_s = 0.14, k_{y2}\rho_s = 0.0$) and non-zonal drift-waves ($k_{x2}\rho_s, k_{y2}\rho_s > 0.0$), where the horizontal and vertical axes correspond to $k_{x2}\rho_s$ and $k_{y2}\rho_s$ respectively.

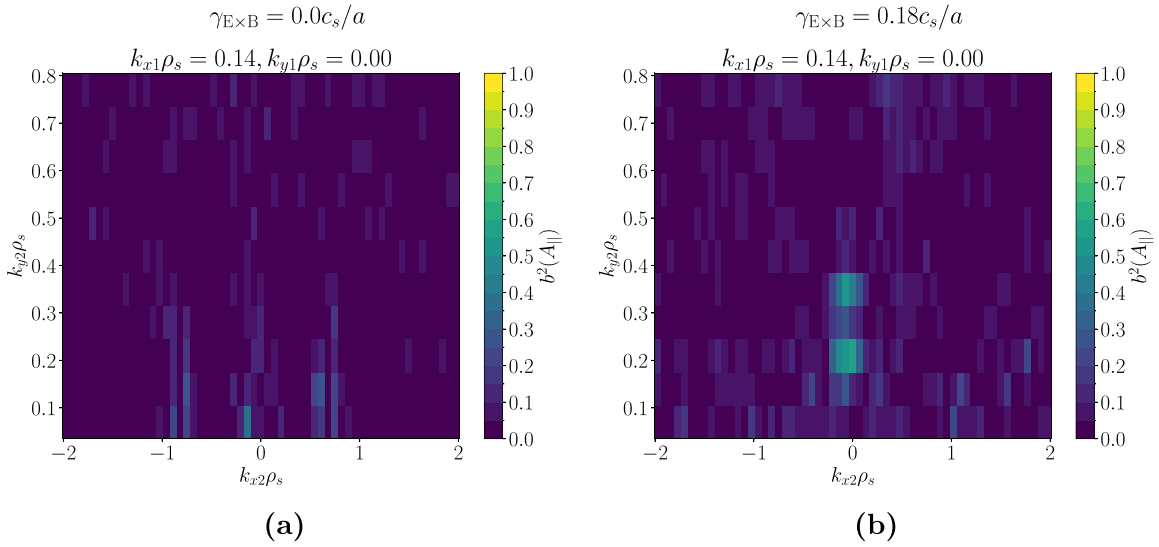

Figure 21. Normalised bicoherence square, b^2, evaluated using $A_\parallel(\theta = 0)$ in the nonlinear phase of the NSTX nonlinear simulation (a) when $\gamma_{E\times B} = 0$, and (b) when $\gamma_{E\times B} = 0.18 c_s/a$. The bicoherence is between a purely zonal mode ($k_{x1}\rho_s = 0.14, k_{y2}\rho_s = 0.0$) and non-zonal drift-waves ($k_{x2}\rho_s, k_{y2}\rho_s > 0.0$), where the horizontal and vertical axes correspond to $k_{x2}\rho_s$ and $k_{y2}\rho_s$ respectively.

without $E \times B$ shear there no significant coupling between $k_x\rho_s$ modes[13] but when it is included there is significant levels of coupling to the stable modes. This weakens the linear drive and causes the heat flux to increase more slowly during this linear phase when the simulation includes $E \times B$ shear.

In the nonlinear saturated state the bicoherence square of the un-normalised $A_{||}(\theta = 0.0)$ is shown in figure 21 with the same wavenumbers. Strikingly, only the simulation with $E \times B$ shear exhibits a strong bicoherence between the zonal mode and the drift wave modes at the peak of the heat flux spectrum, $(k_{x2}\rho_s = 0.14 - 0.35, k_{y2}\rho_s = 0.0)$, indicating that $E \times B$ shear couples these linearly driven modes to more damped regions of the spectrum. A peak is seen in the case without $E \times B$ shear at $k_{x2}\rho_s = 0.75$ which corresponds to the first connected mode connected to $k_x\rho_s = 0.0$ given the box size.

5. Conclusion

This work has helped understand the local plasma equilibrium conditions under which MTM transport should be more susceptible to suppression by perpendicular $E \times B$ sheared flows, and shown that this can be identified linearly from the θ_0 dependence of the linear growth rate.

[13] The most significant coupling in the linear phase without $E \times B$ shear occurs along the $k_{x2}\rho_s = -0.14$ axis, which when coupled to $k_{x1}\rho_s = 0.14$ corresponds to $k_{x3}\rho_s = 0.0$ which is the largest component.

A recent linear theory of MTMs, Hardman *et al* [22], valid for $\beta_e \sim \sqrt{m_e/m_i}$, shows that the MTM growth rate depends on the parameter $\beta_{\text{eff}}(\theta_0)$, and in this paper we have used local gyrokinetic calculations to compare $\gamma^{\text{MTM}}(\theta_0)$ with $\beta_{\text{eff}}(\theta_0)$ for a number of local equilibria from ST plasmas.

In a local MAST equilibrium with $q = 1.08$ and $\hat{s} = 0.34$, γ^{MTM} is weakly dependant on θ_0 and $\beta_{\text{eff}}(\theta_0)$ follows a similar trend. Parameter scans demonstrate that γ^{MTM} is a unique function of β_{eff}, as predicted by Hardman *et al*, indicating that the theory captures the key properties of these linear modes. Nonlinear simulations of this equilibrium confirmed that $E \times B$ shear had little impact on the predicted transport, in line with the weak dependence of γ^{MTM} on θ_0. However when $\hat{s}$ is artificially increased there is a large increase to the predicted heat flux at $\gamma_{E\times B} = 0$. When $E \times B$ shear is included, there is then a significant reduction in the heat flux as expected given the stability in θ_0.

In an NSTX local equilibrium with higher safety factor, $q = 1.71$, and higher magnetic shear, $\hat{s} = 1.70$, the MTMs have larger growth rates and are unstable up to a higher k_y. For $k_y\rho_s > 0.5$, γ^{MTM} is unstable over a narrow window around $\theta_0 = 0$, and the growth rate drops steeply as θ_0 increases, with $\beta_{\text{eff}}(\theta_0)$ having a very similar character. A more detailed study demonstrates that this is due to $k_\perp$ increasing more rapidly along the field line at higher $\hat{s}$ (or finite θ_0); this limits the parallel extent of $A_{||}$ (from Ampère's law) and the radial displacement of the perturbed magnetic field that provides the linear drive.

At lower k_y, however, MTMs become unstable with an additional peak in $\gamma^{\text{MTM}}(\theta_0)$ at $\theta_0 = \pi$ and this feature is not captured by the theory. In this theory the contributions from $J_\perp$ are excluded using the low β ordering. However, this term is related to the size of $\beta(qR/a)^2$ and therefore a low β can be offset by a higher qR/a. Scans were shown illustrating that as $\beta(qR/a)^2$ and thus the relative size of $J_\perp$ is reduced, the second peak on the inboard side disappears, indicating a breaking of the orderings that can occur at higher q or R/a, even at low β, like in the NSTX equilibrium.

In nonlinear simulations, Q_e matches the experimental flux when equilibrium $E \times B$ shear is included[14], and Q_e is an order of magnitude lower than the result of the $\gamma_{E\times B} = 0$ simulation. This mitigation by $E \times B$ shear of the nonlinear MTM heat flux, is as expected given the strong dependence of γ^{MTM} on θ_0 for the dominant modes at $k_y\rho_s > 0.5$. In a nonlinear simulation for the same surface at an artificially lower $\hat{s}$, where γ^{MTM} is much more weakly dependent on θ_0, it is found that the (modest) saturated fluxes are largely insensitive to $E \times B$ shear. This is line with expectations from similar models of turbulence suppression of ITG via a 'Waltz rule' [33]. Bicoherence analysis demonstrates that, in both linear and nonlinear phases, $E \times B$ shear increases the strength of coupling between transport carrying finite k_y drift modes and zonal modes, providing a route from linearly driven to linearly damped modes that can assist turbulence saturation.

[14] This improves on previous simulations that only matched experiment if $E \times B$ shear was neglected [13].

The parameter β_{eff} from recent theory by Hardman *et al* is useful for describing MTMs in regimes where $q \sim 1$, but as q increases it is not able model the non-monotonic behaviour of $\gamma^{\text{MTM}}(\theta_0)$ due to the regime being outside the low β orderings of the model which was used to exclude $J_\perp$ as $(\nabla \cdot J_\perp)/(\nabla \cdot J_{||}) \propto \beta(qR/a)^2$. This also has implications for conventional aspect ratio devices as similar behaviour was also found at higher R/a. Reactor relevant STs will likely aim to operate with $q_{\text{min}} > 2.0$ [26, 34], so this inboard destabilisation may be seen. While increasing $\hat{s}$ opens the door to flow shear suppression of the turbulent fluxes, it simultaneously increases the overlap of magnetic islands by reducing the spacing between rational surfaces, and enhances electron heat transport from stochastic fields. Towards the edge of the reactor, q and $\hat{s}$ should be higher than in the core, so $E \times B$ shear could be more important in this region. Although reactor relevant regimes will be highly self-organised, current profile tailoring can allow for finer control of q and $\hat{s}$ making it a relevant tool in optimising the confinement properties of a future reactor.

Acknowledgments

The authors would like to thank Walter Guttenfelder for providing the NSTX data, Stuart Henderson and Martin Valovič for assisting in generating the MAST data, Francesco Palermo for useful discussions and Jason Parisi for his comments. We would also like to thank Emily Belli and Jeff Candy for assisting with the saturation of MTM simulations performed here. Simulations have been performed on the Marconi National Supercomputing Consortium CINECA (Italy) under the project QLTURB. This work was performed using resources provided by the Cambridge Service for Data Driven Discovery (CSD3) operated by the University of Cambridge Research Computing Service (www.csd3.cam.ac.uk), provided by Dell EMC and Intel using Tier-2 funding from the Engineering and Physical Sciences Research Council (capital Grant EP/T022159/1), and DiRAC funding from the Science and Technology Facilities Council (www.dirac.ac.uk). This work was supported by the Engineering and Physical Sciences Research Council [EP/R034737/1].

Appendix. Convergence of nonlinear simulations in resolution

The convergence of the MTM simulations in $k_y\rho_s$ for the MAST and NSTX simulations are demonstrated here. Figure A1(a) shows a time trace of the electron heat flux from the original MAST simulation without $E \times B$ shear on a grid with 24 $k_y\rho_s$ modes and 384 $k_x\rho_s$ modes shown in blue. Figure A1(a) demonstrates that this is sufficient to capture the peak in the $k_y\rho_s$ spectrum. Increasing the number of $k_y\rho_s$ modes to 32 at the same box size, shown in orange, shows a significant increase in heat flux which initially suggests that the simulation may not be resolved. However, when the number of $k_x\rho_s$ modes is also increased to 512 at fixed box size,

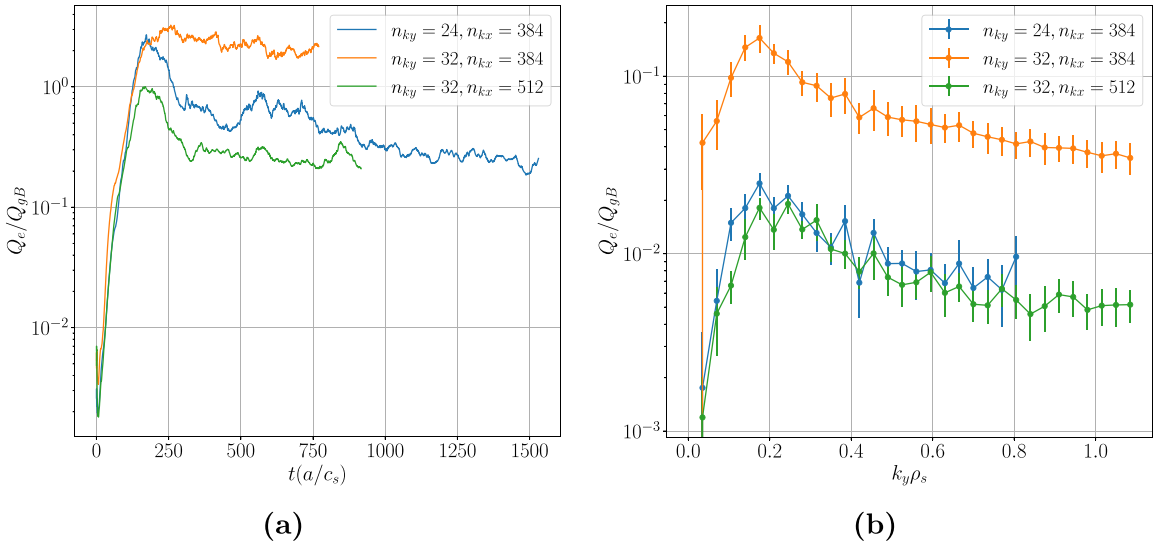

Figure A1. Resolution scan of the MAST equilibrium without $E \times B$ with a varied number of $k_y\rho_s$ and $k_x\rho_s$ grid points showing (a) time trace of the electron heat flux and (b) $k_y\rho_s$ spectrum of the electron heat flux.

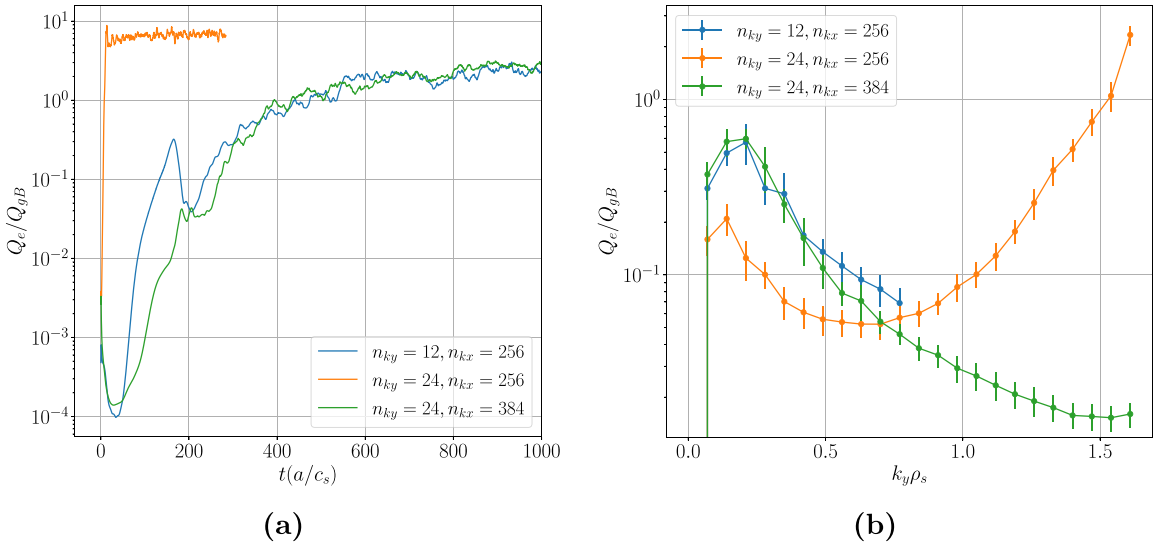

Figure A2. Resolution scan of the NSTX equilibrium with $E \times B$ with a varied number of $k_y\rho_s$ and $k_x\rho_s$ grid points showing (a) time trace of the electron heat flux and (b) $k_y\rho_s$ spectrum of the electron heat flux.

shown in green, then the heat flux amplitude and $k_y\rho_s$ spectrum matches the simulation at the lower resolution in both $k_y\rho_s$ and $k_x\rho_s$. This is likely due to higher $k_y\rho_s$ modes having finer radial structure meaning a larger number of $k_x\rho_s$ modes is needed to capture they behaviour and saturation correctly.

Similarly for the NSTX simulation with $E \times B$ shear, figure A2(a) shows the electron heat flux for the case with 12 $k_y\rho_s$ modes and 256 $k_x\rho_s$ modes in blue. A simulation with double of number $k_y\rho_s$ at the same box size shown in orange, which saturates at a much higher level of heat flux, but figure A2(b) clearly shows the $k_y\rho_s$ flux spectrum is peaking at the highest $k_y\rho_s$. When the number of $k_x\rho_s$ grid points is also increased in tandem from 256 to 384, shown in green, the flux spectrum and overall level of transport matches the simulation with fewer $k_y\rho_s$ and $k_x\rho_s$ modes.

Although the higher $k_y\rho_s$ modes are not contributing significantly to the overall flux in the resolved simulations, when included it is critical to include more $k_x\rho_s$ modes to capture them accurately, given the fine structure of MTMs in $k_x\rho_s$.

ORCID iDs

B.S. Patel https://orcid.org/0000-0003-0121-1187
M.R. Hardman https://orcid.org/0000-0001-5152-3061
D. Kennedy https://orcid.org/0000-0001-7666-782X
M. Giacomin https://orcid.org/0000-0003-2821-2008
D. Dickinson https://orcid.org/0000-0002-0868-211X
C.M. Roach https://orcid.org/0000-0001-5856-0287

References

[1] Patel B.S., Dickinson D., Roach C.M. and Wilson H.R. 2022 Linear gyrokinetic stability of a high β non-inductive spherical tokamak *Nucl. Fusion* **62** 016009

[2] Kennedy D., Giacomin M., Casson F.J., Dickinson D., Hornsby W.A., Patel B.S. and Roach C.M. 2023 Electromagnetic gyrokinetic instabilities in STEP *Nucl. Fusion* **63** 126061

[3] Giacomin M., Kennedy D., Casson F.J., Ajay C.J., Dickinson D., Patel B.S. and Roach C.M. 2024 On electromagnetic turbulence and transport in STEP *Plasma Phys. Control. Fusion* **66** 055010

[4] Wilson H.R., Chapman I.T., Denton T., Morris W., Patel B.S., Voss G.M. and Waldon C. 2020 STEP - on the pathway to fusion commercialization *Commercialising Fusion Energy* p 818

[5] Doerk H., Jenko F., Görler T., Told D., Pueschel M.J. and Hatch D.R. 2012 Gyrokinetic prediction of microtearing turbulence in standard tokamaks *Phys. Plasmas* **19** 055907

[6] Applegate D.J., Roach C.M., Cowley S.C., Dorland W.D., Joiner N., Akers R.J., Conway N.J., Field A.R., Patel A. and Valovic M. 2004 Microstability in a MAST-like high confinement mode spherical tokamak equilibrium *Phys. Plasmas* **11** 5085–94

[7] Valovič M., Akers R., De Bock M., McCone J., Garzotti L., Michael C., Naylor G., Patel A., Roach C.M. and Scannell R. 2011 Collisionality and safety factor scalings of H-mode energy transport in the MAST spherical tokamak *Nucl. Fusion* **51** 073045

[8] Guttenfelder W., Candy J., Kaye S.M., Nevins W.M., Bell R.E., Hammett G.W., LeBlanc B.P. and Yuh H. 2012 Scaling of linear microtearing stability for a high collisionality national spherical torus experiment discharge *Phys. Plasmas* **19** 022506

[9] Dickinson D., Roach C.M., Saarelma S., Scannell R., Kirk A. and Wilson H.R. 2013 Microtearing modes at the top of the pedestal *Plasma Phys. Control. Fusion* **55** 074006

[10] Hatch D.R., Kotschenreuther M., Mahajan S.M., Pueschel M.J., Michoski C., Merlo G., Hassan E., Field A.R., Frassinetti L. and Giroud C. 2021 Microtearing modes as the source of magnetic fluctuations in the JET pedestal *Nucl. Fusion* **61** 036015

[11] Drake J.F. and Lee Y.C. 1977 Kinetic theory of tearing instabilities *Phys. Fluids* **20** 1341–53

[12] Kaye S.M., Gerhardt S., Guttenfelder W., Maingi R., Bell R.E., Diallo A., LeBlanc B.P. and Podesta M. 2013 The dependence of H-mode energy confinement and transport on collisionality in NSTX *Nucl. Fusion* **53** 063005

[13] Guttenfelder W., Candy J., Kaye S.M., Nevins W.M., Wang E., Zhang J., Bell R.E., Crocker N.A., Hammett G.W. and LeBlanc B.P. 2012 Simulation of microtearing turbulence in national spherical torus experiment *Phys. Plasmas* **19** 056119

[14] Guttenfelder W., Candy J., Kaye S.M., Nevins W.M., Wang E., Bell R.E., Hammett G.W., LeBlanc B.P., Mikkelsen D.R. and Yuh H. 2011 Electromagnetic transport from microtearing mode turbulence *Phys. Rev. Lett.* **106** 155004

[15] Giacomin M., Dickinson D., Kennedy D., Patel B.S. and Roach C.M. 2023 Nonlinear microtearing modes in MAST and their stochastic layer formation *Plasma Phys. Control. Fusion* **65** 095019

[16] Doerk H., Jenko F., Pueschel M.J. and Hatch D.R. 2011 Gyrokinetic microtearing turbulence *Phys. Rev. Lett.* **106** 155003

[17] Burrell K.H. 1997 Effects of E$\times$ B velocity shear and magnetic shear on turbulence and transport in magnetic confinement devices *Phys. Plasmas* **4** 1499–518

[18] Davies R., Dickinson D. and Wilson H. 2022 Kinetic ballooning modes as a constraint on plasma triangularity in commercial spherical tokamaks *Plasma Phys. Control. Fusion* **64** 105001

[19] Roach C.M. *et al* 2009 Gyrokinetic simulations of spherical tokamaks *Plasma Phys. Control. Fusion* **51** 124020

[20] Pueschel M.J., Hatch D.R., Görler T., Nevins W.M., Jenko F., Terry P.W. and Told D. 2013 Properties of high-β microturbulence and the non-zonal transition *Phys. Plasmas* **20** 102301

[21] Ajay C.J., McMillan B. and Pueschel M.J. 2022 Microtearing turbulence saturation via electron temperature flattening at low-order rational surfaces (arXiv:2207.09211v3)

[22] Hardman M.R., Parra F.I., Patel B.S., Roach C.M., Ruiz J.R., Barnes M., Dickinson D., Dorland W., Parisi J.F. and St-Onge D. 2023 New linear stability parameter to describe low-β electromagnetic microinstabilities driven by passing electrons in axisymmetric toroidal geometry *Plasma Phys. Control. Fusion* **65** 045011

[23] Candy J. and Staebler G.M. 2016 Crucial role of zonal flows and electromagnetic effects in ITER turbulence simulations near threshold *26th IAEA Fusion Energy Conf., Kyoto, Japan (17–22 October 2016)*

[24] Miller R.L., Chu M.-S., Greene J.M., Lin-Liu Y.R. and Waltz R.E. 1998 Noncircular, finite aspect ratio, local equilibrium model *Phys. Plasmas* **5** 973–8

[25] Arbon R., Candy J. and Belli E.A. 2020 Rapidly-convergent flux-surface shape parameterization *Plasma Phys. Control. Fusion* **63** 012001

[26] Patel B.S. 2021 Confinement physics for a steady state net electric burning spherical tokamak *PhD Thesis*

[27] Patel B.S. *et al* 2024 Pyrokinetics - a python library to standardise gyrokinetic analysis *J. Open Source Softw.* **9** 5866

[28] Hallatschek K. and Dorland W. 2005 Giant electron tails and passing electron pinch effects in tokamak-core turbulence *Phys. Rev. Lett.* **95** 055002

[29] Hardman M.R., Parra F.I., Chong C., Adkins T., Anastopoulos-Tzanis M.S., Barnes M., Dickinson D., Parisi J.F. and Wilson H. 2022 Extended electron tails in electrostatic microinstabilities and the nonadiabatic response of passing electrons *Plasma Phys. Control. Fusion* **64** 055004

[30] Candy J. and Belli E.A. 2018 Spectral treatment of gyrokinetic shear flow *J. Comput. Phys.* **356** 448–57

[31] Rechester A.B. and Rosenbluth M.N. 2020 Electron heat transport in a tokamak with destroyed magnetic surfaces *Hamiltonian Dynamical Systems* (CRC Press) pp 684–7

[32] Cziegler I. 2011 Turbulence and transport phenomena in edge and scrape-off-layer plasmas *PhD Thesis*

[33] Waltz R.E., Dewar R.L. and Garbet X. 1998 Theory and simulation of rotational shear stabilization of turbulence *Phys. Plasmas* **5** 1784–92

[34] Tholerus E., Casson F.J., Marsden S., Wilson T., Brunetti D., Fox P., Freethy S., Hender T.C., Henderson S.S. and Hudoba A. 2024 Flat-top plasma operational space of the STEP power plant *Nucl. Fusion* **64** 106030